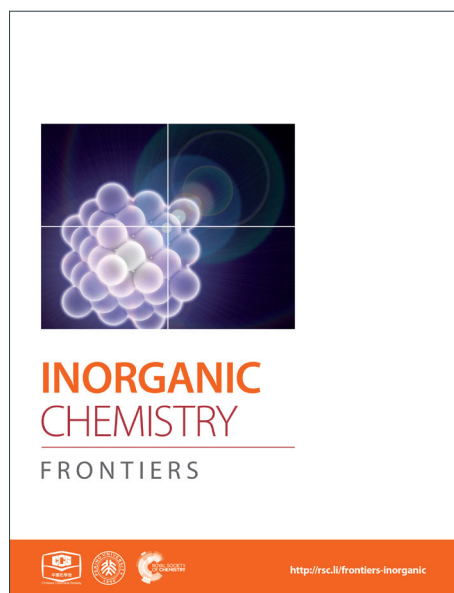
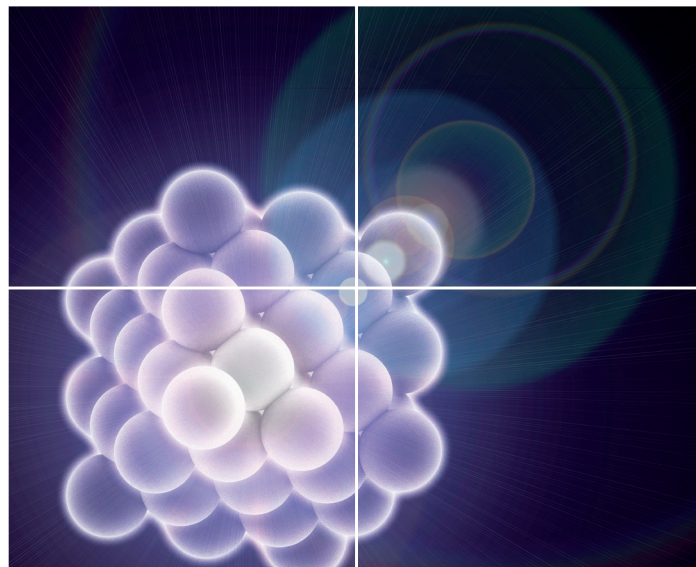


INORGANIC CHEMISTRY

FRONTIERS

Accepted Manuscript



This is an *Accepted Manuscript*, which has been through the Royal Society of Chemistry peer review process and has been accepted for publication.

Accepted Manuscripts are published online shortly after acceptance, before technical editing, formatting and proof reading. Using this free service, authors can make their results available to the community, in citable form, before we publish the edited article. We will replace this *Accepted Manuscript* with the edited and formatted *Advance Article* as soon as it is available.

You can find more information about *Accepted Manuscripts* in the [Information for Authors](#).

Please note that technical editing may introduce minor changes to the text and/or graphics, which may alter content. The journal's standard [Terms & Conditions](#) and the [Ethical guidelines](#) still apply. In no event shall the Royal Society of Chemistry be held responsible for any errors or omissions in this *Accepted Manuscript* or any consequences arising from the use of any information it contains.



Journal Name

ARTICLE

Graphene Oxide and Reduced Graphene Oxide Hybrids with Spin Crossover Iron(III) Complexes†

Received 00th January 20xx,
Accepted 00th January 20xx

DOI: 10.1039/x0xx00000x

www.rsc.org/

Yusuke Murashima^a, Mohammad Razaul Karim^b, Naoto Saigo^a, Hiroshi Takehira^a, Ryo Ohtani^a, Masaaki Nakamura^a, Michio Koinuma^a, Leonard F. Lindoy^c, Keita Kuroiwa,^d Shinya Hayami^{a,e,*}

Graphene (rGO) based hybrid material exhibiting electrical conductivity and spin crossover (SCO) behavior is reported. The non-conductive [Fe(qnal)₂]_nGO (**1 GO**) and [Fe(qsal)₂]_nGO (**2 GO**) hybrids have been prepared by employing the electrostatic interaction between the negatively charged graphene oxide (GO) nanosheet and the respective iron(III) complex cations in [Fe(qnal)₂]⁺Cl⁻ and [Fe(qsal)₂]⁺Cl⁻. The conductive [Fe(qnal)₂]_nrGO (**1 rGO**) and [Fe(qsal)₂]_nrGO (**2 rGO**) hybrids were obtained by thermal reduction of **1 GO** and **2 GO**. **1 GO** and **1 rGO** exhibit SCO behavior, and **1 rGO** also shows a light induced excited spin state trapping (LIESST) effect. Thus, in **1 rGO** the electrical conductivity of rGO and the SCO behavior of [Fe(qnal)₂]⁺ coexist in a single structure. We propose that the observed cooperativity for the rGO nanosheet-bound iron(III) [Fe(qnal)₂]⁺ SCO material occurs through formation of large domains via π-π stacking between the graphene skeleton and the [Fe(qnal)₂]⁺ cations.

Introduction

Reported strategies for combining electrical conductivity with magnetism in hybrid materials involve the combination of magnetic ingredients with a conductive organic/inorganic platform by chemical bond formation, columbic attachment or by layer by layer assembly of the functional species within a porous polymeric framework.^{1,2} In particular, aggregation through non-covalent self-assembly of multi-components to form stable functional molecular materials has received wide interest, as the properties of the components being preserved largely.³ The layering of individual functional materials to form multifunctional hybrids has been successfully adopted for obtaining coalescence between ferromagnetism and metallic conductivity, paramagnetism and superconductivity and ferromagnetism and superconductivity.⁴⁻⁶ In most of these systems magnetic nanoparticles are physically trapped in an appropriate conductive substrate either by stable sandwich formation or through the trapping of the functional components in a folded dispersion phase.⁷ Due to the near homogenous height profile of the conductive mesoporous dispersion phase and its limited interface with the magnetic species, magnetic ordering is largely retained, resulting in the magnetic properties being preserved. In this context, there has been considerable interest for using reduced

graphene oxide (rGO) as a thin, conductive two dimensional dispersed phase.⁸ An additional advantage of using rGO is the possibility for RKKY exchange between graphene's *p*-orbital based electrons and the magnetic entities, which could further enhance magnetic ordering.^{9,10} However, there are inherent difficulties in embedding spin crossover (SCO) materials in such a conductive matrix.

SCO represents magnetic behavior involving the transition of an electron (or electrons) between high spin (HS) and low spin (LS) metal states and is commonly observed for first row transition metal complexes with 3dⁿ (n = 4-7) electronic configurations when they are exposed to external stimuli such as temperature, pressure, magnetic field or light.¹¹ Depending on the extent of cooperativity between the molecules, solid state SCO behavior can be gradual or abrupt. Cooperativity, reflecting the presence of significant intermolecular interaction between the SCO molecules is highly desirable as it induces abrupt SCO behavior (all the molecules in a sample undergo their spin transitions simultaneously) giving rise to hysteresis loops. Such behavior is important in terms of possible applications such as data storage, magnetic switching and optical devices. However, achieving such cooperativity among SCO molecules is not easy, as achieving simultaneous electron transitions across all molecules in a non-homogenous system (with respect to ligand field, special arrangement or dimensionally controlled alignment) is difficult. Considering the role of intermolecular interactions in inducing spin transitions, it was proposed theoretically (and experimentally confirmed) that cooperativity is enhanced by designing polymeric structures, in which the active sites are linked to each other through chemical bridges.¹²⁻¹⁷ The SCO behavior of a complex is well documented to be affected significantly by ligand modification or by interaction of the complex with other materials. However, the generation of additional functionality (e.g. electrical conductivity) in a SCO system by direct elaboration of the system lies beyond theoretical prediction at the present time.

^a Department of Chemistry, Graduate School of Science and Technology, Kumamoto University, 2-39-1 Kurokami, Chuo-ku, Kumamoto 860-8555, Japan.

^b Department of Chemistry, School of Physical Sciences, Shahjalal University of Science & Technology, Sylhet-3114, Bangladesh.

^c School of Chemistry, The University of Sydney, NSW 2006, Australia.

^d Department of Nanoscience, Faculty of Engineering, Sojo University, 4-22-1 Ikeda, Nishi-ku, Kumamoto 860-0082, Japan.

^e Institute of Pulsed Power Science (IPPS), Kumamoto University, 2-39-1 Kurokami, Chuo-ku, Kumamoto 860-8555, Japan.

† Electronic Supplementary Information (ESI) available: See DOI: 10.1039/x0xx00000x

Even though the design of SCO materials with other desired chemical or physical properties has long been a major focus in hybrid materials research,^{18,19} it has only been possible to combine magnetism and SCO in recent times,^{20,21} with very few materials being developed that combine SCO and electrical conductivity in a single platform.²²⁻²⁸ In most cases discrete entities are combined by coulombic attraction (rather than covalent linkage). For example, the use of π stacking and electrostatic attraction resulted in conductive SCO hybrids based on the redox active $[\text{Ni}(\text{dmit})_2]^-$ anion and the spin crossover $[\text{Fe}(\text{sal}_2\text{-trien})]^+$ complex cation.²⁹ Another example exploited the synergism between the electrical conductivity of stacks of $[\text{Ni}(\text{dmit})_2]^-$ in electrocrystallized $[\text{Fe}(\text{qsal})_2][\text{Ni}(\text{dmit})_2]_3 \text{CH}_3\text{CN} \cdot \text{H}_2\text{O}$ and the SCO of $[\text{Fe}(\text{qsal})_2]^+$.³⁰ Although there exist reports of cationic complex SCO behaviour coupled with anionic metal complex conduction, no hybrids based on rGO or any other purely organic framework are known.

In view of the above, we initially considered combining the SCO nature of $[\text{Fe}(\text{qsal})_2]^+$ or $[\text{Fe}(\text{qnal})_2]^+$ (qsal and qnal are the abbreviations of the deprotonated Hqsal (N-(8-quinoly)salicylalimine) and Hqnal (1-((8-quinolinylimino)methyl)-2-naphthalenol), respectively as shown in Figure 1) with the conductivity of rGO. rGO is similar to graphene, which is a well documented electronic conductor³¹ and $[\text{Fe}(\text{qsal})_2]^+$ and $[\text{Fe}(\text{qnal})_2]^+$ are both reported SCO entities.^{32,33} The SCO behavior of $[\text{Fe}(\text{qsal})_2]^+$ and $[\text{Fe}(\text{qnal})_2]^+$ in the presence of various counter anions has been studied extensively while both rGO and GO have perfect two dimensional structures at room temperature.³⁴

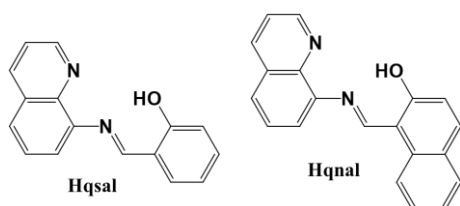
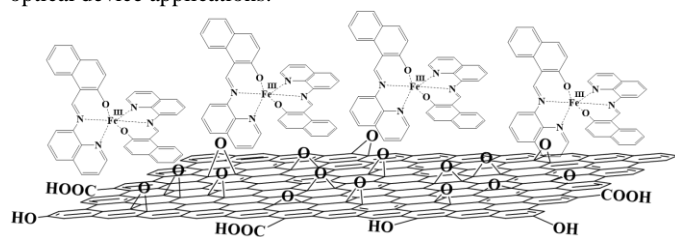


Figure 1 Structures of the ligands, Hqsal and Hqnal.

In the present study, the combination of $[\text{Fe}(\text{qsal})_2]^+$ and $[\text{Fe}(\text{qnal})_2]^+$ with negatively charged GO resulted in the formation of $[\text{Fe}(\text{qsal})_2]_n\text{GO}$ (**1 GO**) and $[\text{Fe}(\text{qsal})_2]_n\text{GO}$ (**2 GO**) as non-conductive GO hybrids (Scheme 1). However, on thermal reduction, these GO hybrids yielded conductive graphene hybrids as $[\text{Fe}(\text{qsal})_2]_n\text{rGO}$ (**1 rGO**) and $[\text{Fe}(\text{qsal})_2]_n\text{rGO}$ (**2 rGO**). In addition, **1 GO** and **1 rGO** each maintain SCO behavior. Furthermore, **1 rGO** also shows a light-induced excited spin state trapping (LIESST) effect. Direct synergy between the electrical conductivity of rGO and the respective spin conversions is shown to involve cooperativity between the SCO molecules embedded on the rGO nanosheets. This result opens a new window for the generation of rGO based hybrid materials for switching and other light driven optical device applications.



Scheme 1 Scheme for electrostatic interaction between positively charged $[\text{Fe}(\text{qnal})_2]^+$ and negatively charged GO, and $[\text{Fe}(\text{qsal})_2]^+$ also is proposed to bind to GO by same interaction.

Experimental

Graphene Oxide Synthesis: Graphene oxide was prepared by modified Hummers' method we reported elsewhere.³⁵ 0.50 g of graphite powder (95%) and 0.5 g of NaNO_3 were mixed in a 200 mL flask placed into an ice bath. 11.5 mL of conc. H_2SO_4 was added and the mixture was stirred for 30 min at 0°C . 1.5 g of KMnO_4 was added slowly with stirring. The mixture was then stirred for 1 h at 35°C . 23 mL of distilled water was slowly added and the mixture was stirred for 30 min at 95°C . The reaction was terminated by adding 100 mL of distilled water followed by 3 mL of 30% H_2O_2 solution. The mixture was cooled and centrifuged at 3000 rpm to remove the supernatant liquid. The remaining solid mixture was washed with 5% HCl acid (1time) distilled water (3 times). The precipitate was dried at 80°C overnight to yield graphite oxide (GtO). 0.2 g of GtO was added into 200 mL deionized water and sonicated for 2 h. This dispersion was centrifuged at 4000 rpm for 1 h and the supernatant liquid was called graphene oxide (GO) dispersion (Figure S1).

Synthesis of $[\text{Fe}(\text{qsal})_2]\text{Cl}$: a solution of 8-aminoquinoline (1.44 g, 10 mmol) and salicylaldehyde (1.22 g, 10 mmol) in methanol (10 mL) was heated to reflux for 1 h. The obtained orange solution was cooled and $\text{FeCl}_3 \cdot 6\text{H}_2\text{O}$ (1.35 g, 5mmol) was added with vigorous stirring. Finally, triethylamine (1.01 g, 10 mmol) was added slowly to the solution. The reaction mixture was stirred at room temperature for 1 h to yield a black precipitate.³⁶

Synthesis of $[\text{Fe}(\text{qnal})_2]\text{Cl}$: a solution of 8-aminoquinoline (0.28 g, 2 mmol) in methanol (20 mL) and 2-hydroxy-1-naphthaldehyde (0.34 g, 2 mmol) in methanol (10 mL) was stirred for 1 h in order to produce Hqnal. Meanwhile, FeCl_3 (0.16 g, 1mmol) was dissolved in absolute methanol (5 mL) containing 2,2'-dimethoxy-propane (2 mL) and warmed at 40°C for 30 min, and was added to the Hqnal in methanol. The micro-crystalline black product was collected by suction and dried in vacuum.³²

Synthesis of GO-SCO hybrids: GO-SCO hybrids, **1 GO** and **2 GO**, were directly precipitated from a mixture of GO dispersion (200 mL) and Iron(III) complexes ($[\text{Fe}(\text{qsal})_2]\text{Cl}$ and $[\text{Fe}(\text{qnal})_2]\text{Cl}$) solution (200 mg in 200 mL methanol) at 25°C for 24 h. The hybrids were washed with water (3 times) with centrifugation (4800 rpm), collected by membrane filter and dried in vacuum (Figure S1).

Synthesis of rGO-SCO hybrids: rGO-SCO hybrids, **1 rGO** and **2 rGO**, were prepared by thermal reduction of GO-SCO hybrids. The powder of GO-SCO hybrids were heated under Argon at 120°C for 24 h (Figure S1).

Physical measurements

To perform transmission electron microscopy (TEM; JEOL, 2000FX, 200 kV), one drop of the aqueous nanosheet suspension was deposited on a holey carbon film. A micro Raman spectrometer (NRS-3100, Jasco, Japan) with a 532 nm excitation source at room temperature was used to collect the Raman spectra. XPS (Thermo Scientific, Sigma Probe) was used to analyze the surface of GO nanosheets. A monochromatized X-ray source (Al K α , $h\nu = 1486.6$ eV) was used for XPS. In this measurement, a Pt substrate (GO/Pt film) was used to determine the fermi level. All measurements were done in a vacuum better than 10^{-7} Pa. Emitted electrons were

detected by a hemispherical energy analyzer equipped with six channeltrons. The powder X-ray diffraction (XRD) patterns were recorded on a Rigaku X-ray diffractometer (RAD-2A with a 2.0 kW CuK α X-ray).

Temperature dependence of the electrical resistivity of a pellet of GO-SCO and rGO-SCO hybrids were measured by a nanovoltmeter (Keithley 2182A Digital Nanovoltmeter) using a four-terminal method in the temperature range of 150-300 K. The conductivities along the surface of GO-SCO hybrids and rGO-SCO hybrids were measured on glass substrate by a two electrode system.

The magnetic susceptibilities for GO-SCO and rGO-SCO hybrids between 2 K and 400 K were measured with a superconducting quantum interference device (SQUID) magnetometer (Quantum Design MPMSXL-5) in an external field of 1 T.

The Mössbauer spectra were measured with a Wissel MVT-1000 Mössbauer spectrometer with a $^{57}\text{Co}/\text{Rh}$ source in the transition mode. All isomer shifts are given relative to $\alpha\text{-Fe}$ at room temperature. Measurements at low temperature were performed with a closed-cycle helium refrigerator cryostat (Iwatani Co., Ltd.).

Result and discussion

The morphologies of the GO and its hybrid derivatives **1 GO** and **2 GO** are illustrated in the TEM images shown in Figures 2(a), (b) and (d). The folded GO nanosheet is darkened in its **1 GO** and **2 GO** hybrids. Following reduction, the randomly distributed dark spots in the former hybrids become denser and more widespread in **1 rGO** and **2 rGO** due to nanoparticles forming on the rGO surface following coagulation of the respective iron complexes (Figure 2(c) and (e)). In **1 GO** and **2 GO** the binding of cations on the negatively charged GO nanosheet is stabilized by charge balance and further coagulation of the metal complexes is inhibited. However, on reduction to rGO, the charge disappears and the hybrids are stabilized by encapsulation of coagulated metal complexes giving rise to the formation of dense and more defined spots. It is also proposed that the secondary positive charge on the metal complex cations is partly balanced by Cl $^{-}$ anions. During reduction electron acceptance also likely results in some secondary charge balance, which aids coagulation. That is, the GO nanosheets trap the SCO molecules by electrostatic interaction (Scheme 1) and after thermal reduction the coagulated mass is sandwiched within the 2D carbon matrix of rGO in each case.

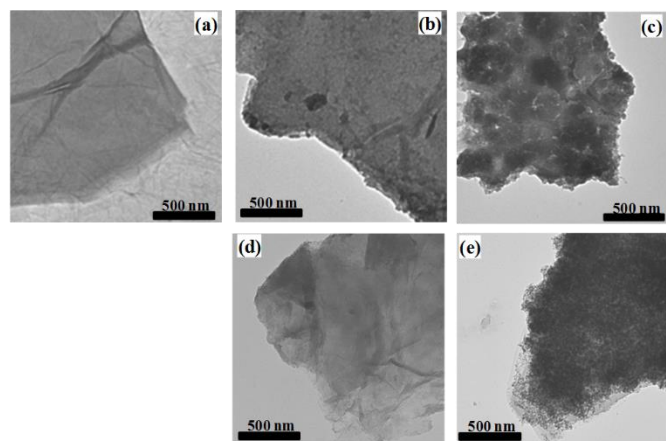


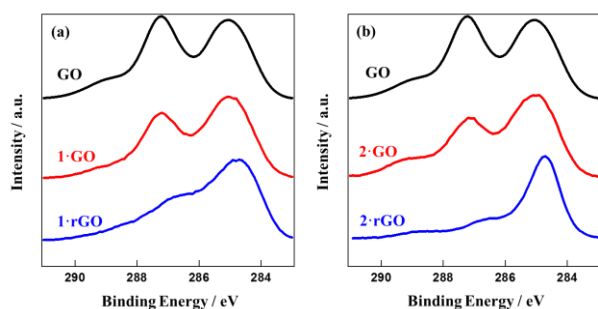
Figure 2 TEM images for (a) GO, (b) **1 GO**, (c) **1 rGO**, (d) **2 GO** and (e) **2 rGO**.

The PXRD pattern of GO shows a characteristic peak at 11.27° (2θ), with a d spacing of 7.83 Å signifying the presence of intercalated oxygen atoms positioned at various oxygenated functional sites (Figure S2).³⁷ Due to the accommodation of [Fe(qnal) $_2$] $^{+}$ and [Fe(qnsl) $_2$] $^{+}$ by the GO nanosheet, the respective d spacing increases to 9.16 and 8.89 Å with the peak positions (2θ) occurring at 9.65° and 9.64° , respectively. When GO is reduced to rGO, the coagulated mass of the respective iron(III) complexes is encapsulated by folded layers of rGO, with the characteristic peak for the oxygenated sites no longer present. In the case of **2 rGO**, a new shallow peak in the high angle region is seen, which is in accord with the lowering of the interlayer distance due to the removal of epoxy sites from some regions of the GO nanosheet during reduction. However, for **1 rGO**, the corresponding shallow peak is not so clear.

The Raman spectra of GO, **1 GO** and **2 GO** are compared in Figure S3. The chemical change corresponding to the conversion of GO to rGO and the coulombic interaction between the GO nanosheet and [Fe(qnal) $_2$] $^{+}$ is reflected by the change in position of the G band and relative heights of the D (1357 cm^{-1}) and G (1591 cm^{-1}) bands; the D and G bands correspond to the breathing mode of A_{1g} and in-plane bond stretching motion of pairs of sp^2 C atoms (E_{2g}) mode, respectively.^{38,39} The G band position for GO shifts to 1593 cm^{-1} in **1 GO** and then to 1589 cm^{-1} on reduction of **1 GO** to **1 rGO**. The slight hardening (shifting of peaks to high frequency region) during the formation of **1 GO** from GO implies a change in the electronic environment due to the resonance through π - π interaction between the organic framework of the iron complex and the GO nanosheet. In this context, it is noted that the presence of an electron rich heteroatom or chemical modification has also been reported to result in such hardening.^{40,41} While **1 GO** is changed to **1 rGO**, the slight softening (shifting of peaks to low frequency region) is an expected consequence of the π - π interaction being lowered. The peak ratio (I_D/I_G) increases from 0.87 in GO to 0.98 in **1 GO** and 1.00 in **1 rGO**. The I_D/I_G is inversely proportional to the extent of the sp^2 C domain. Therefore, an increase in this value signifies the fragmentation of large sp^2 islands of GO during the metal complex attachment and subsequent reduction.^{42,43} In addition, the D band intensity is related to the extent of defects in the GO plane.⁴⁴ These defects arise from the metal complex deposition on the GO nanosheet. In case of **2 GO**, the change in Raman parameters are very similar to those discussed above. Here, the G band positions are 1591 , 1595 and 1599 cm^{-1} for GO, **2 GO** and **2 rGO**, respectively. The respective I_D/I_G ratios are, 0.87, 0.91 and 1.04.

GO exhibits two characteristic peaks near 285 and 287 eV in their XPS spectra (Figure 3). Oxygen functional groups in GO present in the form of epoxide ($-\text{O}-$) and hydroxyl ($-\text{OH}$) groups with XPS peak positions in the range 286.8 - 287.0 eV as well as carbonyl ($-\text{C}=\text{O}$), carboxyl ($-\text{COOH}$) groups between 287.8 - 288.0 eV and 289.0 - 289.3 eV, respectively.^{45,46} The peak for oxygenated C1s is narrower and higher compared to the C1s peak for unoxidized carbon sites ($-\text{C}-\text{C}-$ and $-\text{C}=\text{C}-$). The relative amounts of $-\text{C}-\text{O}$, $-\text{C}-\text{O}-\text{C}-$, $-\text{C}=\text{O}$ and $\text{O}=\text{C}-\text{O}-$ functional sites are 3.9, 32.3, 6.3 and 7.5%, respectively. The ratio of area under the peak for oxygenated

C1s to the area of oxygenated and un oxygenated C1s carbon sites reveals that the carbon to oxygen ratio is around 7 : 3 and comply with some previous report.⁴⁷ In Figure 3(a) the carbon and oxygen contents are changed in **1 GO** as 72.1 and 24.79% and in **1 rGO** as 75.55 and 21.48%. The carbon content increase due to the attachment of $[\text{Fe}(\text{qnal})_2]^+$ on GO and rGO. For reduction the carbon content increase further due to the breaking of epoxy sites and removal of other oxygen functional groups. The N, Fe, and Cl contents in **1 GO** and **1 rGO** are 1.97, 0.48, 0.5 and 2.05, 0.45, 0.35%, respectively. The N : Fe : Cl ratio is almost 4 : 1 : 1 in each



sample confirming the presence of Cl^- anion and in keeping with undissociated $[\text{Fe}(\text{qnal})_2]^+$ ion being present on the GO nanosheet. We propose that the Cl^- anion becomes attached to GO through some non-specific adsorption related to achieving charge balance. On reduction, the decrease in peak height near 287 eV is in accord with the destruction of some epoxy and hydroxyl groups having occurred. However, following reduction these peaks have not completely disappeared thus indicating that some epoxy and hydroxyl groups remain intact. **2 GO** and **2 rGO** hybrids also exhibited close to similar behavior (Figure 3(b)).

Figure 3 XPS spectra for (a) GO (black), **1 GO** (red) and **1 rGO** (blue), and (b) GO (black), **2 GO** (red) and **2 rGO** (blue).

While GO is a well known insulator with respect to electron conduction, conductivity is recovered after reduction.⁴⁸ Temperature dependent electrical resistivities for **1 rGO** and **2 rGO** were measured in the temperature range of 150-300 K employing a HUSO HECS 9065 conductometer using the conventional four-probe method (Figure S4). Both hybrids show semiconducting behavior. For **1 rGO** the resistivity at 150 K is $2.70 \times 10^5 \Omega \text{ cm}$ and this reduces exponentially with temperature. At 300 K the resistivity is almost zero. For **2 rGO** a similar trend is observed with the resistivity being 95 and $0 \Omega \text{ cm}$ at 150 and 300 K, respectively. The conductive natures of all the hybrids were further probed by observing the current (I) - voltage (V) curves for the hybrids before and after thermal reduction. The I-V curves are presented in Figure 4. The unreduced hybrids show zero conductivity regardless of the applied voltage. However, for **1 rGO** and **2 rGO** the current increases linearly with voltage. At 1 V, the electron conductivities for **1 rGO** and **2 rGO** are 18 and 680 μA , respectively.

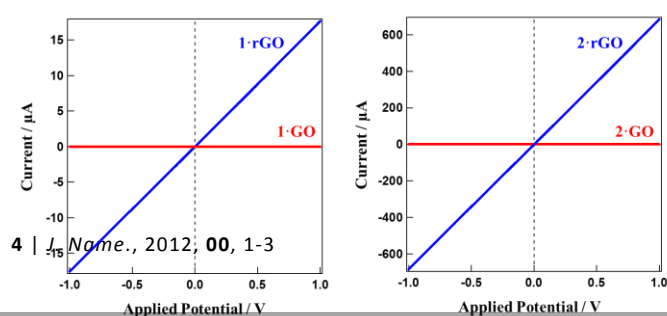


Figure 4 The related I-V curve showing the conductivity of the hybrids for (a) **1 GO** and **1 rGO**, and (b) **2 GO** and **2 rGO**.

The $\chi_g T$ value versus temperature behavior for **1 GO** is shown in Figure S5. The value of $\chi_g T$ for **1 GO** remains constant at $1.65 \times 10^{-3} \text{ cm}^3 \text{ K g}^{-1}$ from 2-180 K. From 180-260 K, $\chi_g T$ rises gradually, then follows a steeper increase beyond 260 K. At 400 K the $\chi_g T$ value reaches $2.28 \times 10^{-3} \text{ cm}^3 \text{ K g}^{-1}$. For **1 rGO**, $\chi_g T$ is $1.9 \times 10^{-3} \text{ cm}^3 \text{ K g}^{-1}$ at 10 K. A gradual increase with constant steep is then observed, with the $\chi_g T$ value reaching $2.5 \times 10^{-3} \text{ cm}^3 \text{ K g}^{-1}$ at 400 K. Both **1 GO** and **1 rGO** displays clear evidence for SCO behavior. However, as both GO and rGO are nanostructured polymers, their size and shape cannot be controlled, and the exact molecular formula (or weight) of the GO hybrids is unable to be calculated. Therefore, in place of emu K mol^{-1} , the magnetic susceptibility is expressed in terms of $\text{cm}^3 \text{ K g}^{-1}$. Though the temperature dependent spin transition is very clear, the fraction of iron(III) in the low and high spin states before and after the spin transition in **1 GO** and **1 rGO** is unable to be calculated from the susceptibility measurement. We also estimated the high-spin (HS) and low-spin (LS) ratio in SCO by means of ^{57}Fe Mössbauer spectra. The temperature dependence of the Mössbauer spectra of **1 GO** is presented in Figure 5. The black dots represent the observed spectra while the blue and red lines represent the simulated LS and HS curves, respectively. The black line represents the sum of the simulated LS and HS curves. The Mössbauer parameters at 300 K for **1 GO** are as following. HS area $A_{\text{HS}} = 61\%$, isomer shift (I.S.) = 0.38 mm s^{-1} , quadrupole splitting (Q.S.) = 0.76 mm s^{-1} , and LS area $A_{\text{LS}} = 39\%$, I.S. = 0.17 and Q.S. = 2.32 . At 5 K, $A_{\text{HS}} = 36.0\%$, I.S. = 0.51 , Q.S. = 0.90 , and $A_{\text{LS}} = 64\%$, I.S. = 0.22 and Q.S. = 2.55 . The HS fraction (γ_{HS}) increases 0.36 to 0.61 on heating (5 - 300 K). In case of **1 rGO**, the Mössbauer parameters at 300 K are as following. $A_{\text{HS}} = 65\%$, I.S. = 0.38 mm s^{-1} and Q.S. = 0.77 mm s^{-1} , and $A_{\text{LS}} = 35\%$, I.S. = 0.17 mm s^{-1} and Q.S. = 2.24 mm s^{-1} . At 5 K, $A_{\text{HS}} = 41\%$, I.S. = 0.51 mm s^{-1} , Q.S. = 0.89 mm s^{-1} , and $A_{\text{LS}} = 59\%$, I.S. = 0.21 mm s^{-1} , Q.S. = 2.52 mm s^{-1} . γ_{HS} increases 0.41 to 0.65 on heating (5 - 300 K). The Mössbauer spectra therefore confirm the temperature dependent SCO of **1 GO** and **1 rGO**. The other hybrids **2 GO** and **2 rGO** were also studied by SQUID and Mössbauer spectra, but exhibited no SCO behavior (Figures S5 and S6). These differences result from the different domains size of $[\text{Fe}(\text{qnal})_2]^+$ and $[\text{Fe}(\text{qsal})_2]^+$ metal complexes cations on GO and rGO. The cation $[\text{Fe}(\text{qnal})_2]^+$ has larger π -conjugated ligand that interacts with GO and rGO strongly. As a result, the domain size of $[\text{Fe}(\text{qnal})_2]^+$ is large on GO and rGO, **1 GO** and **1 rGO** show SCO behavior. On the other hand, the domain size of $[\text{Fe}(\text{qsal})_2]^+$ is smaller because of smaller π -conjugated ligand on GO and rGO, and **2 GO** and **2 rGO** don't show the SCO behavior.

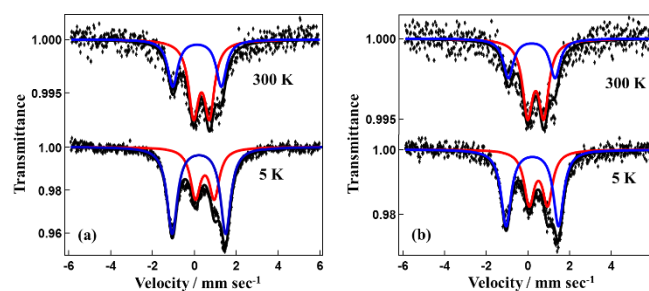
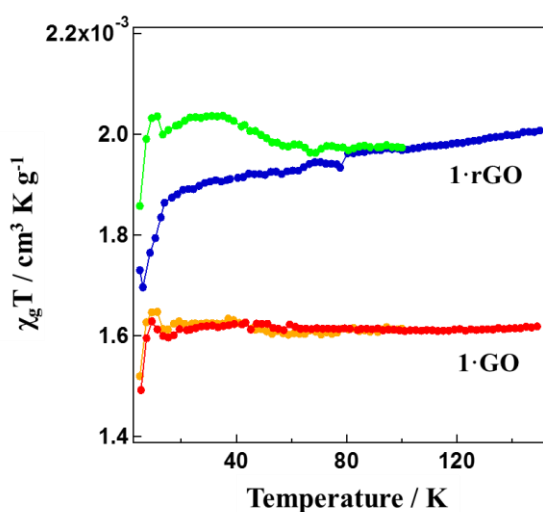


Figure 5 Mössbauer spectra for (a) **1 GO** and (b) **1 rGO**.

The LIESST experiments for **1 GO** and **1 rGO** were carried out employing an illuminating microconductor laser (1000 nm) coupled via an optical fiber to the cavity of a SQUID magnetometer (Figure 6). The sample was placed on the edge of the optical fiber. On illuminating **1 rGO** at 5 K, an increase in its magnetization was observed, suggesting that the photo-induced metastable HS state can be trapped in the **1 rGO** hybrid. Relaxation of this metastable state to the ground LS state occurred at about 50 K. For **1 GO**, the LIESST effect wasn't able to observe. TEM image of **1 rGO** shows the randomly distributed dark spots demonstrating the existence of gathered complexes in which the metal complexes have shorter intermolecular distance than **1 GO**, which revealed that a clustering of the complexes on rGO is a key to produce the LIESST effect of **1 rGO**.

**Figure 6** $\chi_g T$ vs T plot for **1 GO** (red) and **1 rGO** (blue). Sample **1 GO** (yellow) and **1 rGO** (green) was warmed after 1000 nm irradiation at 5 K.

It is worth to state that the coexistence of SCO and electrical conductivity in any graphene hybrid is highly fascinating, as the property coalescence is resulted from sustaining the components functionality. As SCO cationic species we chose classical Fe^{3+} complexes of N-donor ligands. The SCO entity $[\text{Fe}(\text{qsal})_2]^+$ and $[\text{Fe}(\text{qnal})_2]^+$ become attached and colagulated on the porous GO and rGO framework without suffering any chemical change. The hybrids take the shapes of SCO nanoparticles dispersed on 2D graphene. As chemical reduction results a coagulated mass of the complex in each case, thermal reduction was employed for the samples to be used for the conductivity measurements. The cations are strongly coupled and arranged closely via π -stacking with rGO matrices. Therefore, the large intramolecular structure transmits the SCO electronic transition quite efficiently within the entire hybrid and signifies the coercive force responsible for the observed SCO behavior. Along with the existence of graphene conductivity the establishment of π -stacking to enhance cooperativity in SCO complexes has been demonstrated to be a successful synthetic strategy for devising GO and rGO based

hybrids. The electrons travel along the GO and rGO nanosheets giving rise to the electronic conductivity. Both the conductivity of rGO and SCO behavior of the $[\text{Fe}(\text{qsal})_2]^+$ and $[\text{Fe}(\text{qnal})_2]^+$ precursors is maintained solely due to the nature of the physical interaction that occurs between these components in the respective hybrid products. That is, the 2D graphene sheet supports polymeric networking between the SCO entities to yield the observed cooperative effect.

Conclusion

We have observed clear evidence for coupling between the electrical properties of rGO and SCO behavior of metal complex in new hybrid materials. The graphene based hybrids **1 GO**, **2 GO**, **1 rGO** and **2 rGO** were synthesized by employing coulombic attraction and through the sandwiching of iron(III) complexes within the folded layers of rGO. While the GO hybrids are insulators, the rGO hybrids are conductors. The hybrids **1 rGO** and **2 rGO** exhibit both the electrical conductivity. Furthermore **1 GO** and **1 rGO** exhibit SCO behavior, and **1 rGO** also show the LIESST effect. We succeeded to control the domain size of metal complexes on GO and rGO. These hybrids belong to the rare category of materials displaying the coexistence of SCO behavior and electrical conductivity. Graphene-based materials with these dual properties are presented here for the first time. We look forward to observing related cooperatively between other SCO entities embedded in GO and rGO nanosheet hybrid materials in the future.

Acknowledgements

This work was supported by KAKENHI Grant-in-Aid for Scientific Research (B) 26288026 and Grant-in-Aid for Scientific Research on Innovative Areas 2506 [Science of Atomic Layers].

Notes and references

1. P. Day, *World Scientific: Singapore*, 2007.
2. M. Clemente-León, E. Coronado, A. Forment-Aliaga, P. Amorós, J. Ramírez-Castellanos, and J. M. González-Calbet, *J. Mater. Chem.*, 2003, **13**, 3089.
3. J. M. Lehn, *Science*, 2002, **295**, 2400.
4. E. Coronado, J. R. Galán-Mascarós, C. J. Gómez-García and V. Lalkhin, *Nature*, 200, **408**, 447.
5. E. Ojima, H. Fujiwara, K. Kato and H. Kobayashi, *J. Am. Chem. Soc.*, 1999, **121**, 5581.
6. E. Coronado, C. Martí-Gastaldo, E. Navarro-Moratalla, A. Ribera, S. J. Blundell and P. J. Baker, *Nat. Chem.*, 2010, **2**, 1031.
7. E. Coronado, M. Giménez-Marqués, C. Martí-Gastaldo, G. M. Espallargas, E. Navarro-Moratalla and J. C. Waerenborgh, *Inorg. Chem.*, 2013, **52**, 8451.
8. M. R. Karim, R. Ohtani, H. Takehira and S. Hayami, *Curr. Inorg. Chem.*, 2014, **4** 191.
9. M. R. Karim, H. Shinoda, M. Nakai, K. Hatakeyama, H. Kamihata, T. Matsui, T. Taniguchi, M. Koinuma, K.

- Kuroiwa, M. Kurmoo, Y. Matsumoto and S. Hayami, *Adv. Funct. Mater.*, 2013, **23**, 323.
10. Y. Murashima, R. Ohtani, T. Matsui, H. Takehira, R. Yokota, M. Nakamura, L. F. Lindoy and S. Hayami, *Dalton Trans.*, 2015, **44**, 5049.
11. P. Gütllich and H. A. Goodwin, *Topics in Current Chemistry*, 2004, **233**, 1.
12. W. Vreugdenhil, J. H. Vandiemmen, R. A. Degraaf, J. G. Haasnoot, A. M. Vanderkraan, O. Kahn and J. Zarembowitch, *Polyhedron*, 1990, **9**, 2971.
13. M. Clemente-León, E. Coronado, M. C. Giménez-López and F. M. Romero, *Inorg. Chem.*, 2007, **46**, 11266.
14. O. Sato, T. Iyoda, A. Fujishima and K. Hashimoto, *Science*, 1996, **272**, 704.
15. V. Niel, J. M. Martínez-Agudo, M. C. Muñoz, A. B. Gaspar and J. A. Real, *Inorg. Chem.*, 2001, **40**, 3838.
16. J.-F. Létard, P. Guionneau, O. Nguyen, J. S. Costa, S. Marcen, G. Chastanet, M. Marchivie and L. Goux-Capes, *Chem. Eur. J.*, 2005, **11**, 4582.
17. W. Kosaka, K. Nomura, K. Hashimoto and S. Ohkoshi, *J. Am. Chem. Soc.*, 2005, **127**, 8590.
18. A. B. Gaspar, V. Ksenofontov, M. Serezyuk and P. Gütllich, *Coord. Chem. Rev.*, 2005, **249**, 2661.
19. V. Niel, A. L. Thompson, M. C. Muñoz, A. Galet, A. E. Goeta and J. A. Real, *Angew. Chem., Int. Ed.*, 2003, **42**, 3760.
20. M. Clemente-León, E. Coronado, M. López-Jordà, J. C. Waerenborgh, C. Desplanches, H. Wang, J.-F. Létard, A. Hauser and A. Tissot, *J. Am. Chem. Soc.*, 2013, **135**, 8655.
21. M. Clemente-León, E. Coronado and M. López-Jordà, *Dalton Trans.*, 2010, **39**, 4903.
22. H. Akamatu, H. Inokuchi and Y. Matsunaga, *Nature*, 1954, **173**, 168.
23. E. Coronado and P. Day, *Chem. Rev.*, 2004, **104**, 5419.
24. L. Ouahab, *Coord. Chem. Rev.*, 1998, **178-180**, 1501.
25. E. Coronado and J. R. Galan-Mascarós, *J. Mater. Chem.*, 2005, **15**, 66.
26. K. Takahashi, H.-B. Cui, Y. Okano, H. Kobayashi, H. Mori, H. Tajima, Y. Einaga and O. Sato, *J. Am. Chem. Soc.*, 2008, **130**, 6688.
27. B. Djukic and M. T. Lemaire, *Inorg. Chem.*, 2009, **48**, 10489.
28. B. Djukic, T. Seda, S. I. Gorelsky, A. J. Lough and M. T. Lemaire, *Inorg. Chem.*, 2011, **50**, 7334.
29. S. Dorbes, L. Valade, J. A. Real and C. Faulmann, *Chem. Commun.*, 2005, **69**, 69.
30. K. Takahashi, H.-B. Cui, Y. Okano, H. Kobayashi, Y. Einaga and O. Sato, *Inorg. Chem.*, 2006, **45**, 5739.
31. A. K. Geim and K. S. Novoselov, *Nat. Mater.*, 2007, **6**, 183.
32. T. Shimizu, Y. Komatsu, H. Kamihata, Y. H. Lee, A. Fuyuhiko, S. Iijima and S. Hayami, *J. Incl. Phenom. Macrocycl. Chem.*, 2011, **71**, 363.
33. S. Hayami, Z. Gu, H. Yoshiki, A. Fujishima and O. Sato, *J. Am. Chem. Soc.*, 2001, **123**, 11644.
34. Y. Zhu, S. Murali, W. Cai, X. Li, J. W. Suk, J. R. Potts and R. S. Ruoff, *Adv. Mater.*, 2010, **22**, 3906.
35. M. R. Karim, K. Hatakeyama, T. Matsui, H. Takehira, T. Taniguchi, M. Koinuma, Y. Matsumoto, T. Akutagawa, T. Nakamura, S.-I. Noro, T. Yamada, H. Kitagawa and S. Hayami, *J. Am. Chem. Soc.*, 2013, **135**, 8097.
36. S. Hayami, K. Hiki, T. Kawahara, Y. Maeda, D. Urakami, K. Inoue, M. Ohama, S. Kawata and O. Sato, *Chem. Eur. J.*, 2009, **15**, 3497.
37. P. Cui, J. Lee, E. Hwang and H. Lee, *Chem. Commun.*, 2011, **47**, 12370.
38. F. Tuinstra and J. L. Koenig, *J. Chem. Phys.*, 1970, **53**, 1126.
39. A. C. Ferrari and J. Robertson, *Phys. Rev. B*, 2000, **61**, 14095.
40. M. C. Hsiao, S. H. Liao, M. Y. Yen, P. I. Liu, N. W. Pu, C. A. Wang and C. C. Ma, *Appl. Mater. Interfaces*, 2010, **2**, 3092.
41. Y. Ikeda, M. R. Karim, H. Takehira, K. Hatakeyama, T. Matsui, T. Taniguchi, M. Koinuma, Y. Matsumoto and S. Hayami, *Chem. Lett.*, 2014, **43**, 486.
42. Z. Zafar, Z. H. Ni, X. Wu, Z. X. Shi, H. Y. Nan, J. Bai and L. T. Sun, *Carbon*, 2013, **61**, 57.
43. R. Podila, J. Chacón-Torres, J. T. Spear, T. Pichler and P. Ayala, *Appl. Phys. Lett.*, 2012, **101**, 123108.
44. M. R. Karim, Y. Ikeda, T. Ide, S. Sugimoto, K. Toda, Y. Kitamura, T. Ihara, T. Matsui, T. Taniguchi, M. Koinuma, Y. Matsumoto and S. Hayami, *New J. Chem.*, 2014, **38**, 2120.
45. T. Szabó, O. Berkesi, P. Forgó, K. Josepovits, Y. Sanakis, D. Petridis and I. Dékány, *Chem. Mater.*, 2006, **18**, 2740.
46. D. W. Boukhvalov and M. I. Katsnelson, *J. Am. Chem. Soc.*, 2008, **130**, 10697.
47. Y. Matsumoto, M. Koinuma, S. Y. Kim, Y. Watanabe, T. Taniguchi, K. Hatakeyama, H. Tateishi and S. Ida, *Appl. Mat. Int.*, 2010, **2**, 3461.
48. D. Chen, H. Feng and J. Li., *Chem. Rev.*, 2012, **112**, 6027.